Available online at www.sciencedirect.com
ScienceDirect
Trans. Nonferrous Met. Soc. China 32(2022) 2494−2509
Transactions of Nonferrous Metals Society of China
www.tnmsc.cn

Effect of Gd on microstructure, mechanical properties, and corrosion behavior of as-homogenized Mg−8Li−3Al−2Zn−0.2Zr alloy

Yue-hua SUN[1], Ri-chu WANG[2], Chao-qun PENG[2], Xiao-feng WANG[2]

1. School of Materials Science and Engineering, Anhui University of Technology, Maanshan 243002, China;
2. School of Materials Science and Engineering, Central South University, Changsha 410083, China

Received 6 August 2021; accepted 29 December 2021

Abstract: The microstructure observation, tensile test, electrochemical measurement, and corrosion morphology characterization were conducted to study the effect of Gd on the microstructure, mechanical properties, and corrosion behavior of as-homogenized Mg−8Li−3Al−2Zn−0.2Zr (LAZ832−0.2Zr) alloy. The addition of trace Gd can improve the mechanical properties of as-homogenized LAZ832−0.2Zr alloy by refining the microstructure, reducing the content of AlLi softening phase, and forming Al_2Gd strengthening phase. Meanwhile, the addition of trace Gd can weaken the microgalvanic corrosion between matrix phase and AlLi phase, inhibit the galvanic corrosion between α-Mg phase and β-Li phase, and result in the formation of dense oxide film containing Gd_2O_3, thereby improving the corrosion resistance of the alloy. When the Gd content is 1.0 wt.%, the alloy shows the best comprehensive properties with the ultimate tensile strength of 189.8 MPa, elongation of 42.3%, and corrosion rate (determined by hydrogen evolution) of 0.86 mm·a^{-1}.

Key words: Mg−Li alloy; rare earth Gd; microstructure; mechanical properties; corrosion behavior

1 Introduction

With the growing shortage of global energy, lightweight has become an urgent demand and development trend in various industrial fields. Mg−Li alloys are the lightest metal structural materials, and their densities are only 1.25−1.65 g/cm^3 [1,2]. Besides, the addition of Li significantly improves the plastic deformation ability by reducing the *c*/*a* axial ratio of Mg lattice and changing the crystal structure from hexagonal close packed (hcp) to body centered cubic (bcc) [3,4]. Therefore, Mg−Li alloys have been favored by various industrial fields especially in aerospace, military, and electronic industries [5,6]. However, low strength and poor corrosion resistance seriously limit the rapid development and wide application of Mg−Li alloys.

Alloying is considered to be an effective method for improving the strength and corrosion resistance of Mg−Li alloys. Al is one of the most important alloying elements in Mg−Li alloys, and it can effectively enhance the alloy strength owing to its large solid solubility in Mg matrix and be easy to form intermetallic compounds with other elements [7,8]. PUGAZHENDHI et al [9] reported that the addition of Al could increase the work hardening and the Mg−8Li−*x*Al (*x*=0, 2, 4, 6) alloys exhibited increasing strength with increasing Al content, but the elongation decreased obviously when the Al content was higher than 4 wt.%. ZHAO et al [10,11] proved that the addition of 3 wt.% Al could lead to a significant improvement in the tensile strength of Mg−Li alloys, which was attributed to the precipitation strengthening effects of Al−Li precipitates and the solid solution strengthening of Al in α-Mg matrix. In addition, the

Corresponding author: Xiao-feng WANG, Tel: +86-13467516329, Fax: +86-731-88836638, E-mail: wangxiaofeng@csu.edu.cn
DOI: 10.1016/S1003-6326(22)65961-2
1003-6326/© 2022 The Nonferrous Metals Society of China. Published by Elsevier Ltd & Science Press

addition of Al to Mg can ennoble corrosion potential and promote the formation of dense oxide film, thus reducing the corrosion rates of Mg alloys [12,13]. Zn has a similar effect on Mg−Li alloys to Al, and difference is that strengthening effect per unit mass is worse than that of Al [14]. Moreover, Zn could have a negative effect on the corrosion resistance of Mg alloys when its content is higher than 2.5 wt.%, so the content of Zn is usually controlled below 2.0 wt.% [12]. In Mg−Li alloys, Al and Zn are added simultaneously as alloying elements to make the most of respective advantages.

In recent years, Mg−Li−Al−Zn alloys have attracted more and more attention due to the excellent mechanical properties. Among them, dual-phase Mg−8Li−3Al−2Zn (LAZ832) alloy has better plasticity than α-Mg single-phase alloy and higher strength than β-Li single-phase alloy, presenting good comprehensive mechanical properties [15,16]. Additionally, our previous studies have shown that dual-phase LAZ832−0.2Zr alloy exhibits good corrosion resistance, but it is far from enough for practical application [17,18]. Rare earth (RE) elements are proven to benefit the mechanical properties and corrosion resistance of dual-phase Mg−Li−Al(−Zn) alloys [19−23]. On the one hand, the addition of rare earth elements can refine grain size, and preferentially combine with Al atom to form Al−RE compounds and decrease the content of AlLi phase, accordingly improving the mechanical properties of alloys [19,20]. On the other hand, the addition of rare earth elements can purify alloy melt, weaken the microgalvanic corrosion, and promote the formation of dense oxide film on alloy surface, thus improving the corrosion resistance of alloys [21−23]. According to the relevant literatures, the researches on the effect of RE on dual-phase Mg−Li−Al(−Zn) alloys are mainly focused on Y, Nd, and Ce, but Gd is paid little attention. Gd element has the same hcp structure as Mg and high solubility (4.53 at.%) in Mg matrix [24]. In addition, Gd has electronegativity and atomic radius similar to Y. Therefore, it is expected that the addition of trace Gd element can improve the mechanical properties and corrosion resistance of dual-phase Mg−Li−Al(−Zn) alloys.

In this work, the dual-phase LAZ832−0.2Zr alloy with good comprehensive properties was taken as the research object to study the effect of Gd on the microstructure and properties, so as to further improve the mechanical properties and corrosion resistance of LAZ832−0.2Zr alloy.

2 Experimental

The LAZ832−xGd−0.2Zr (x=0, 0.5, 1.0, 1.5, 2.0, 2.5, wt.%) alloys used in this work were melted from pure Mg (>99.9 wt.%), pure Li (>99.9 wt.%), pure Al (>99.9 wt.%), pure Zn (>99.9 wt.%), Mg−30wt.%Gd and Mg−30wt.%Zr master alloys under the protection of pure argon atmosphere in a vacuum induction furnace. After mixing and holding at 730 °C for 10 min, the melt was poured into a pure tantalum mold with a diameter of 80 mm and naturally cooled to ambient temperature. Then, the cast ingots were homogenized at 280 °C for 24 h to make microstructure and composition more homogeneous. Table 1 lists the chemical composition and density of alloys, which were determined with an inductively coupled plasma optical emission spectroscope (ICP-OES) and an electronic density balance (AEL−200), respectively.

Phase composition was analyzed with D/Max 2500 X-ray diffraction (XRD) at a step size of 0.02°

Table 1 Chemical composition and density of experimental alloys

Alloy	Actual composition/wt.%						Density/(g·cm^{-3})
	Li	Al	Zn	Gd	Zr	Mg	
LAZ832−0.2Zr	8.03	2.96	2.01	0.00	0.18	Bal.	1.514
LAZ832−0.5Gd−0.2Zr	8.01	2.91	2.00	0.47	0.21	Bal.	1.521
LAZ832−1.0Gd−0.2Zr	8.06	2.97	2.06	1.02	0.20	Bal.	1.529
LAZ832−1.5Gd−0.2Zr	7.95	3.04	2.05	1.47	0.16	Bal.	1.536
LAZ832−2.0Gd−0.2Zr	7.98	2.98	2.04	1.96	0.18	Bal.	1.542
LAZ832−2.5Gd−0.2Zr	8.02	3.01	2.04	2.43	0.16	Bal.	1.551

and a constant scan rate of 8 (°)/min. Microstructure was observed with an optical microscope (OM, Leica-DM6000M), a transmission electron microscope (TEM, Tecnai G2 F20 S-Twin), and a scanning microscope (SEM, Quanta−200) equipped with energy dispersive X-ray spectroscope (EDS). Tensile tests were conducted with a tensile tester (MTS−858) at a tensile rate of 2 mm/min, and the dimensions of tensile specimens were 6 mm in diameter and 30 mm in gauge length according to standard GB/T 228.1—2010.

Electrochemical tests were performed in 3.5 wt.% NaCl solution by a Multi Autolab/M204 electrochemistry workstation, and a classical three-electrode cell was used with saturated calomel electrode (SCE) as reference electrode, platinum foil as counter electrode, and testing specimen with an exposed area of 1 cm^2 as working electrode. Potentiodynamic polarization curves were recorded from the cathodic side at a constant scan rate of 1 mV/s. Electrochemical impedance spectroscopy (EIS) was conducted over a frequency ranging from 10^5 Hz to 10^{-2} Hz with a perturbation amplitude voltage of 5 mV. Hydrogen evolution was evaluated by the gas collection. The testing specimens with an exposed area of 1 cm^2 were immersed in 3.5 wt.% NaCl solution for 15 d, and the volume of hydrogen released per day was recorded. The corrosion morphologies with and without corrosion products were observed with SEM, and the surface oxide films of alloys after immersion for 24 h were analyzed with X-ray photoelectron spectroscopy (XPS, ESCALAB 250Xi).

3 Results and discussion

3.1 Microstructure

Figure 1 shows the XRD patterns of as-homogenized LAZ832−xGd−0.2Zr alloys. It is seen that all LAZ832−xGd−0.2Zr alloys contain α-Mg, β-Li, AlLi, and $MgLi_2Al$ phases, and they are typical α-Mg+β-Li dual-phase alloys. The addition of Gd results in the formation of Al_2Gd phase (fcc structure, a=7.9025 Å). With the increase of Gd content, the content of Al_2Gd phase increases gradually, while the content of AlLi phase decreases slightly. The preferential nucleation of Al_2Gd phase consumes Al atoms owing to the largest electronegativity difference between Al (1.61) and Gd (1.20), leading to the decrease in the content of AlLi phase. Therefore, a part of Gd added into alloys exists in matrix in form of solid solution, and the remaining forms Al_2Gd compound.

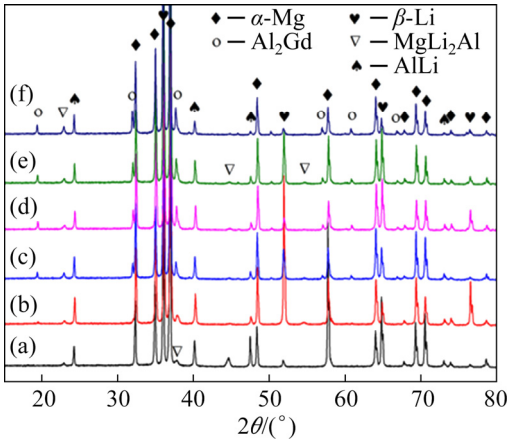

Fig. 1 XRD patterns of as-homogenized LAZ832−xGd−0.2Zr alloys: (a) x=0; (b) x=0.5; (c) x=1.0; (d) x=1.5; (e) x=2.0; (f) x=2.5

Figure 2 depicts the OM micrographs of as-homogenized LAZ832−xGd−0.2Zr alloys. All LAZ832−xGd−0.2Zr alloys are typical α-Mg+β-Li dual-phase alloys, which is consistent with the XRD results and Mg−Li binary phase diagram. In as-homogenized LAZ832−0.2Zr alloy, α-Mg phase is long strip-shaped and β-Li phase fills in the space among α-Mg phases. After adding Gd element, the long-strip α-Mg phase gradually changes to become round-like and fine needle-like microstructure. When the Gd content is 1.5 wt.%, the refining effect of α-Mg phase is the most obvious. With the further increase of Gd content, the fine needle-like α-Mg phase disappears, and the round-like α-Mg phase coarsens and becomes longer. In addition, it can be seen that the content of α-Mg phase decreases slightly while that of β-Li phase increases with increasing Gd content, but the change is not significant. The effect of Gd element on the microstructure of dual-phase LAZ832−0.2Zr alloy is similar to that of Y element, which can refine the microstructure significantly, make the long-strip α-Mg phase change to round-like shape, and inhibit the formation of α-Mg phase [19,25]. The refining effect of Gd is mainly due to the fact that the addition of Gd can promote grain nucleation and inhibit grain growth. First, Gd has the same hcp structure as α-Mg phase and high melting point (1313 °C), and it can act as the core of non-uniform nucleation for α-Mg phase during solidification to

increase the nucleation rate. Moreover, Gd is a kind of surface-active element, which is easy to accumulate in the front of solid/liquid interface during solidification and results in constitutional undercooling, thereby increasing nucleation rate. Besides, the Al_2Gd phase with high melting point (1525 °C) formed in alloys can inhibit the growth of α-Mg phase [26]. Therefore, the addition of trace Gd can refine the grain size and make α-Mg phase convert from long-strip shape to small round-like and fine needle-like shape.

Figure 3 shows the SEM micrographs of as-homogenized LAZ832−xGd−0.2Zr alloys, and the EDS results of second phases marked by red crosses are listed in Table 2. Clearly, there are lots of second phases besides light-gray α-Mg and dark-gray β-Li matrix phases in alloys. In as-homogenized LAZ832−0.2Zr alloy, the filamentous phase is full of α-Mg matrix, and the blocky phase mainly distributes in β-Li matrix and along the α-Mg/β-Li phase interface. The corresponding EDS results of blocky phases show that they mainly

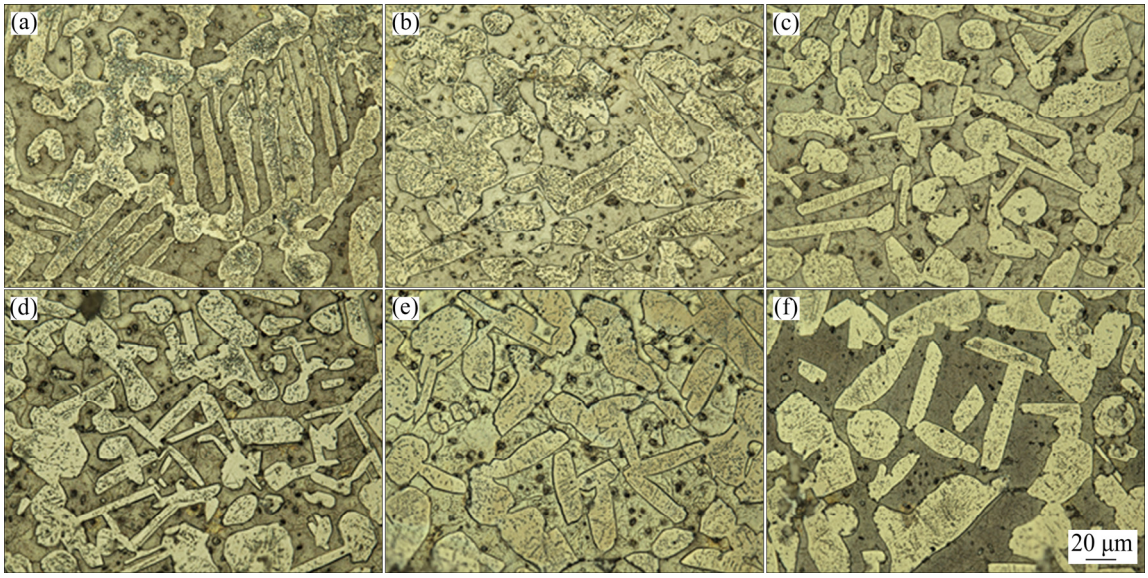

Fig. 2 OM images of as-homogenized LAZ832−xGd−0.2Zr alloys: (a) x=0; (b) x=0.5; (c) x=1.0; (d) x=1.5, (e) x=2.0; (f) x=2.5

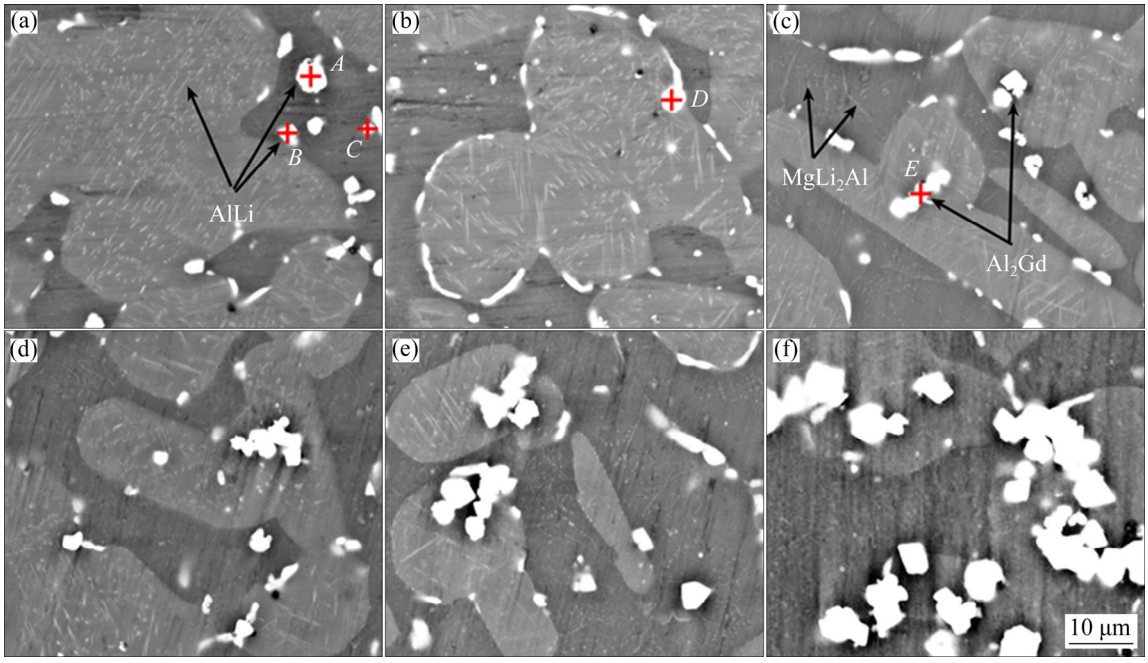

Fig. 3 SEM micrographs of as-homogenized LAZ832−xGd−0.2Zr alloys: (a) x=0; (b) x=0.5; (c) x=1.0; (d) x=1.5; (e) x=2.0; (f) x=2.5

Table 2 EDS results of second phases marked by red crosses in Fig. 3

Point	Content/at.%			
	Mg	Al	Zn	Gd
A	66.91	20.03	13.06	0.00
B	65.61	20.56	13.83	0.00
C	66.12	20.16	13.72	0.00
D	63.83	23.01	1.82	11.34
E	58.36	26.13	2.26	13.25

contain Mg, Al, and Zn elements. According to the XRD results and previous literatures, both the filamentous and blocky phases are AlLi phase [27,28]. After adding Gd element, a kind of polygonal phase is formed in α-Mg matrix. The corresponding EDS results show that these polygonal phases are rich in Mg, Al, and Gd elements, and their Al/Gd atom ratios are close to 2:1. Combined with the XRD results, the polygonal phase is identified as Al_2Gd phase. As the Gd content increases, the amounts of both filamentous and blocky AlLi phases decrease, and the filamentous AlLi phase distributing in α-Mg matrix shows a tendency of coarsening. However, the amount of polygonal Al_2Gd phase gradually increases with the increase of Gd content, and the Al_2Gd phase appears serious segregation when the Gd content is more than 1.0 wt.%. The segregation of Al_2Gd phase leads to the decrease of heterogeneous nucleation core and weakens the inhibition effect of grain growth, which is the main reason for the coarsening of α-Mg matrix with excessive Gd content. Additionally, it can be found that many tiny particulate and thread-like phases distribute in β-Li matrix of all alloys. According to the XRD results and previous literatures [16,27], these particulate and thread-like phases are $MgLi_2Al$ phases.

Figures 4(a, f) display the HAADF-STEM images of as-homogenized LAZ832−0.2Zr and LAZ832−1.0Gd−0.2Zr alloys, respectively. The α-Mg/β-Li phase interface can be clearly seen and

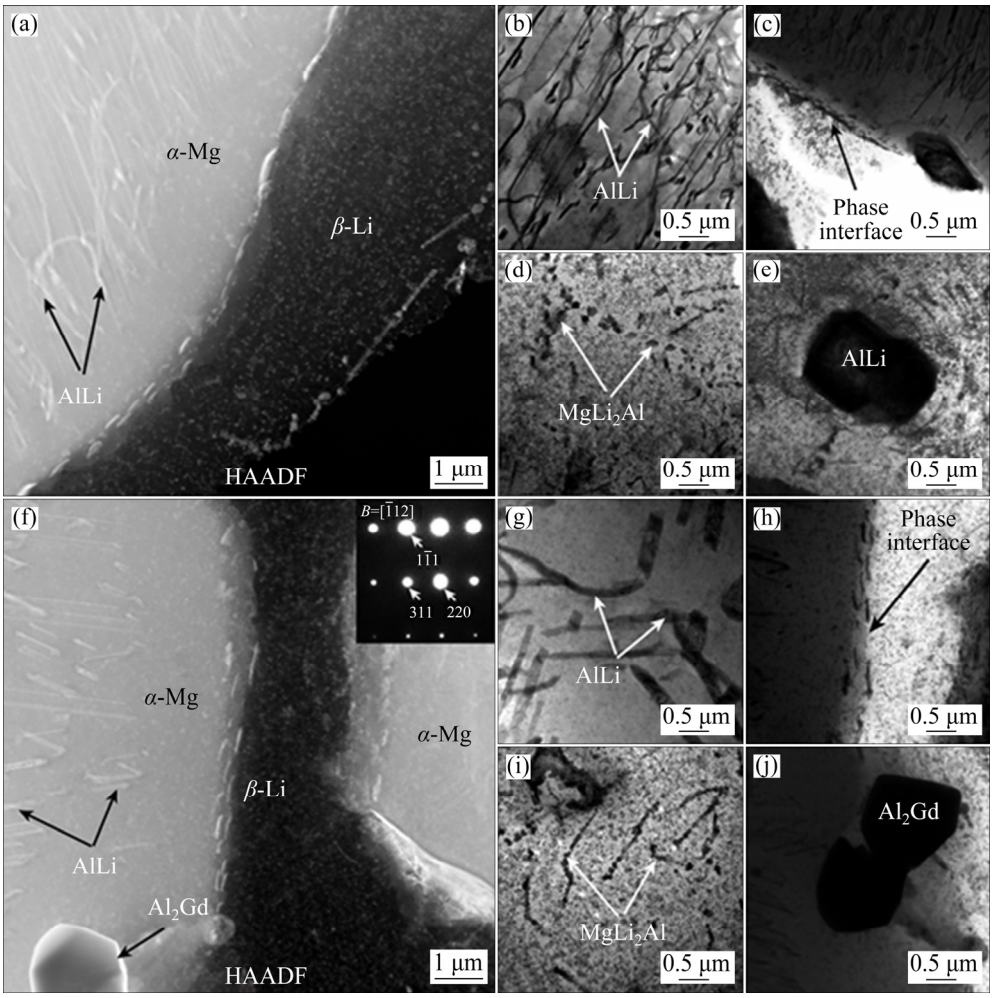

Fig. 4 TEM micrographs of as-homogenized LAZ832−0.2Zr (a−e) and LAZ832−1.0Gd−0.2Zr (f−j) alloys

there are many short rod-like phases distributing along the α-Mg/β-Li phase interface. This short rod-like phase should be AlLi or $MgLi_2Al$ phase according to the XRD results. The filamentous AlLi phase in α-Mg matrix does not reach the phase interface directly, but stops at the region 0.5−2.0 μm away from the phase interface. In as-homogenized LAZ832−0.2Zr alloy shown in Figs. 4(b−e), the filamentous AlLi phase in α-Mg matrix is slender and disordered with a width of 30−120 nm, the blocky AlLi phase in β-Li matrix is relatively large with a size of about 2.5 μm, and nanoscale round-like $MgLi_2Al$ particles is observed in β-Li matrix. Some of these round-like $MgLi_2Al$ particles are dispersed and exist alone, while others are connected in series to form thin lines. In as-homogenized LAZ832−1.0Gd−0.2Zr alloy, the filamentous AlLi phase in α-Mg matrix is short and thick with a width of 250−600 nm, and round-like $MgLi_2Al$ particles in β-Li matrix are slightly smaller than those in Fig. 4(d). Besides filamentous AlLi phase, blocky AlLi phase, and round-like $MgLi_2Al$ particles, the polygonal Al_2Gd phase is observed in α-Mg matrix and its diffraction pattern is shown in the upper right corner of Fig. 4(f).

3.2 Mechanical properties

Figure 5 shows the stress−strain curves of as-homogenized LAZ832−xGd−0.2Zr alloys, and their mechanical properties are listed in Table 3. Both the ultimate tensile strength (UTS) and elongation (δ) of alloys increase first and then decrease with the increase of Gd content. When the Gd content is 1.0 wt.%, the alloy exhibits the best mechanical properties with the UTS and δ of 189.8 MPa and 42.3%, which are improved by 7.4% and 37.8% compared with those of as-homogenized LAZ832−0.2Zr alloy, respectively. The results reveal that the addition of trace Gd element is beneficial to the improvement of the mechanical properties of LAZ832−0.2Zr alloy, which can be explained as follows. First, the addition of trace Gd element can refine the grain size and α-Mg phase, and make long-strip α-Mg phase change to small round-like and fine needle-like microstructure. Grain refinement is an effective method to improve the strength and elongation of alloy simultaneously. Compared with long-strip α-Mg phase, the small round-like and fine needle-like α-Mg phase can reduce the stress concentration during the tensile testing, which is conducive to the improvement of elongation. Second, the addition of Gd element results in the formation of Al_2Gd phase and the decrease of AlLi phase. AlLi phase in Mg−Li alloys is a softening phase, while Al_2Gd phase is a stable strengthening phase with high hardness [29−31]. Therefore, Al_2Gd phase acts as barrier to prevent dislocation movement during tensile process, and thereby increases the strength of alloy. Third, the solubility of Gd (4.53 at.% at 548 °C) in Mg is large, and a great number of Gd atoms appear in alloys in the form of solid solution. Therefore, Gd can enhance the strength of alloy by solution strengthening effect. However, the addition of excessive Gd leads to the serious segregation of Al_2Gd phase, as shown in Fig. 3. During tensile process, stress concentration is easy to occur at the segregation region of Al_2Gd phase, thus reducing the strength

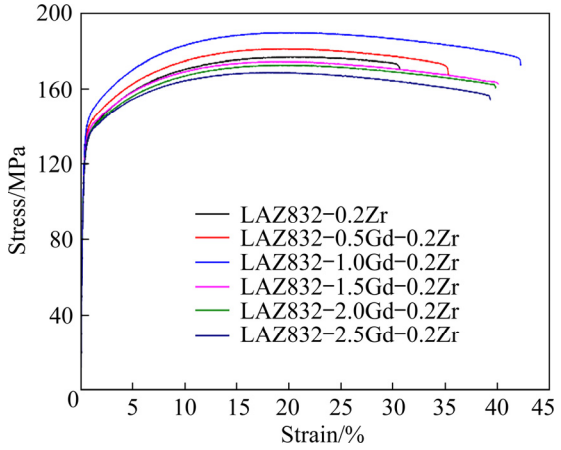

Fig. 5 Stress−strain curves of as-homogenized LAZ832−xGd−0.2Zr alloys

Table 3 Mechanical properties of as-homogenized LAZ832−xGd−0.2Zr alloys

Gd content/ wt.%	UTS/MPa		δ/%	
	Mean	SD	Mean	SD
0	176.8	1.3	30.7	0.6
0.5	181.1	1.1	35.3	0.4
1.0	189.8	1.3	42.3	0.5
1.5	174.4	1.2	40.1	0.6
2.0	172.5	0.8	39.8	0.5
2.5	168.6	1.1	39.3	0.7

SD refers to the standard deviation from the mean value

and elongation of alloys. Furthermore, the addition of Gd element slightly decreases the content of α-Mg phase while increases the content of β-Li phase, which also leads to the decrease of tensile strength.

Figure 6 illustrates the fracture morphologies of as-homogenized LAZ832−xGd−0.2Zr alloys. It can be seen from Figs. 6(a, g) that the fracture morphology of as-homogenized LAZ832−0.2Zr alloy contains obvious cleavage steps and massive dimples, showing the mixed characteristics of cleavage fracture and dimple fracture. Many blocky AlLi particles are observed at the bottom of dimples, and some of them are broken. This fracture mechanism is microvoid coalescence fracture in which microcracks are formed by the connection of microvoids, and dimple is its basic feature. The microvoids are formed attributed to the rapture of second phase caused by stress concentration and the separation of second phase from matrix caused by deformation incompatibility. According to Fig. 3, these AlLi particles mainly distribute in β-Li matrix and along the α-Mg/β-Li phase interface. Therefore, the fracture mode of β-Li matrix is microvoid coalescence fracture. Compared with β-Li matrix, α-Mg matrix with hcp structure has high hardness and poor plastic deformation ability, and is prone to cleavage fracture. As the Gd content increases, the number of cleavage step decreases, while the number of dimple increases. In the enlarged fracture morphology of as-homogenized LAZ832−1.0Gd−0.2Zr alloy (Fig. 6(h)), there are some Al_2Gd particles at the bottom of dimples besides AlLi particles. The Al_2Gd phase distributes in α-Mg matrix, as shown in Fig. 3, which indicates that the formation of Al_2Gd phase results in the transformation of fracture mode for α-Mg matrix from cleavage fracture to microvoid coalescence fracture. This is also the reason why the addition of trace Gd leads to the increase of elongation. When

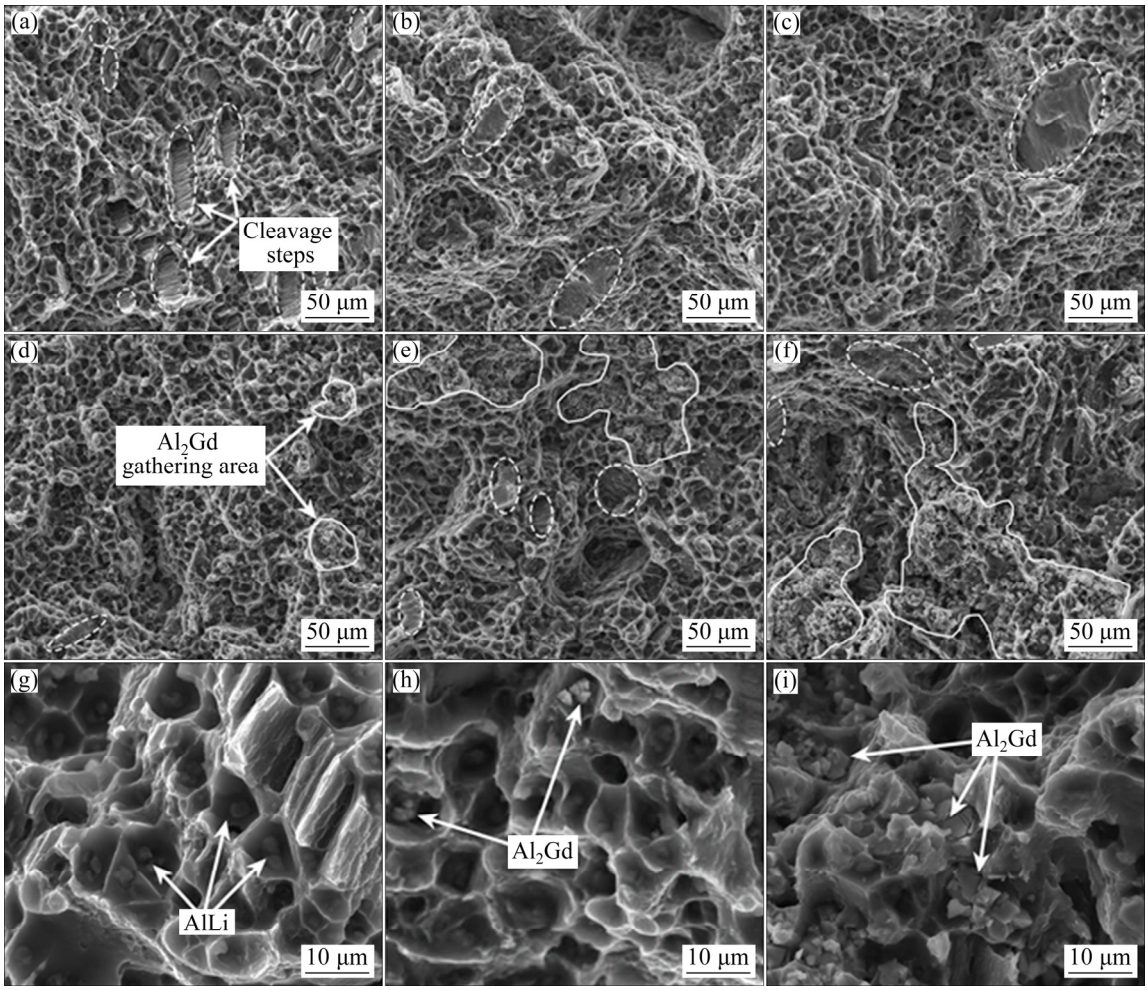

Fig. 6 Fracture morphologies of as-homogenized LAZ832−xGd−0.2Zr alloys: (a) x=0; (b) x=0.5; (c) x=1.0; (d) x=1.5; (e) x=2.0; (f) x=2.5; (g, h, i) Enlarged views of (a, c, f), respectively

the Gd content increases to 1.5 wt.%, the segregation regions of Al_2Gd phase are observed at the fracture surface of alloy. With the further increase of Gd content, the segregation of Al_2Gd phase becomes more serious. The fracture surface of as-homogenized LAZ832−2.5Gd−0.2Zr alloy (Fig. 6(i)) exhibits the serious segregation regions of Al_2Gd phase, in which large stress concentration leads to premature failure and dimples become no longer obvious in these regions. Therefore, the segregation of Al_2Gd phase is the reason why the strength and elongation of alloy decrease due to the addition of excessive Gd element.

3.3 Corrosion behavior

Figure 7 presents the polarization curves of as-homogenized LAZ832−*x*Gd−0.2Zr alloys in 3.5 wt.% NaCl solution. All polarization curves are composed of anode branch and cathode branch, and controlled by activation. Table 4 lists the corresponding Tafel fitting results obtained by CorrView software using the cathodic branches. As the Gd content increases, the corrosion potentials (φ_{corr}) of as-homogenized LAZ832−*x*Gd−0.2Zr alloys increase first and then decrease, while the corrosion current densities (J_{corr}) decrease first and then increase. This indicates that the addition of trace Gd can reduce the corrosion driving force and improve the corrosion resistance of the alloy, while the addition of excessive Gd can lead to the increase of corrosion driving force and the deterioration of corrosion resistance. When the Gd content is 1.0 wt.%, the alloy has the most positive corrosion potential (−1.584 V) and the smallest corrosion current density (16.28 μA/cm^2), which are 64 mV more positive and 34.92 μA/cm^2 lower than those of as-homogenized LAZ832−0.2Zr alloy, respectively. Therefore, as-homogenized LAZ832−1.0Gd−0.2Zr alloy exhibits the smallest corrosion driving force and the best corrosion resistance.

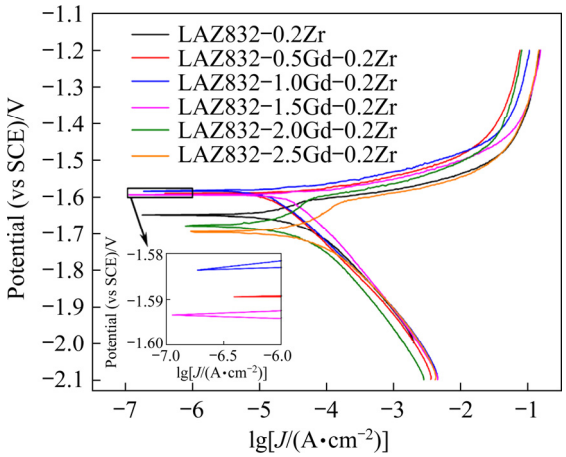

Fig. 7 Polarization curves of as-homogenized LAZ832−*x*Gd−0.2Zr alloys in 3.5 wt.% NaCl solution

Table 4 Tafel fitting results of as-homogenized LAZ832−*x*Gd−0.2Zr alloys

Gd content/ wt.%	φ_{corr}(vs SCE)/ V	J_{corr}/ (μA·cm^{-2})	b_c/ (V·decade^{-1})
0	−1.648	51.20	0.200
0.5	−1.589	17.08	0.183
1.0	−1.584	16.28	0.176
1.5	−1.594	38.04	0.217
2.0	−1.678	53.47	0.216
2.5	−1.697	88.64	0.198

Figure 8 presents electrochemical impedance spectroscopies of as-homogenized LAZ832−*x*Gd−0.2Zr alloys at open circuit potential in 3.5 wt.% NaCl solution. The Nyquist plots (Fig. 8(a)) of all alloys contain a high-frequency capacitive loop, a medium-frequency capacitive loop, and a low-frequency inductive loop. It is consistent with the feature of the Bode plots of angle versus frequency

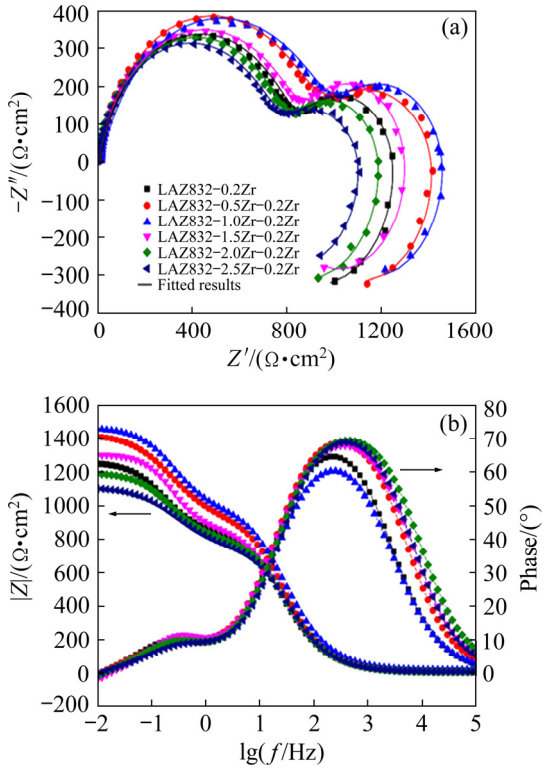

Fig. 8 Electrochemical impedance spectroscopies of as-homogenized LAZ832−*x*Gd−0.2Zr alloys in 3.5 wt.% NaCl solution at 25 °C: (a) Nyquist plots; (b) Bode plots

in (Fig. 8(b)) that there are two positive peaks and one negative valley. The equivalent circuit in Fig. 9 is used for fitting these EIS data and the corresponding fitting results are listed in Table 5. R_s is the solution resistance. R_t and CPE_{dl} represent charge transfer resistance and double layer capacitance, respectively, which are used to describe the high-frequency capacitive loop. R_f and CPE_f are film resistance and film capacitive, respectively, which are used to describe the medium-frequency capacitive loop. The inductive resistance (R_L) and inductance (L) are used to describe the low-frequency inductive loop which might be related to the breakdown of protective film and the nucleation of local corrosion (such as pitting corrosion) [32,33]. It can be clearly seen that the R_t values of as-homogenized LAZ832−xGd−0.2Zr alloys increase first and then decrease with the increase of Gd content, and reach the maximum value when the Gd content is 1.0 wt.%. Compared with other alloys, as-homogenized LAZ832−1.0Gd−0.2Zr alloy has the largest R_t value of 994.6 Ω·cm^2, which indicates that the alloy exhibits higher charge transfer resistance and weaker chemical activity. In the Bode plots shown in Fig. 8(b), the impedance modulus $|Z|$ of as-homogenized LAZ832−1.0Gd−0.2Zr alloy is higher than that of other alloys in the whole frequency range, indicating that the alloy has the slowest anodic dissolution rate and shows the best corrosion resistance. Therefore, the addition of trace Gd can effectively enhance charge transfer resistance and impedance modulus, decrease anodic dissolution rate, and accordingly improve the corrosion resistance of as-homogenized LAZ832−0.2Zr alloy. However, the addition of excessive Gd accelerates the anodic dissolution and deteriorates corrosion resistance of alloy. This is in agreement with the corrosion resistance of alloy reflected by the corrosion current density in Table 4. Additionally, as the Gd content increases, both the R_f and R_L values of as-homogenized LAZ832−xGd−0.2Zr alloys increase first and then decrease, and simultaneously reach their maximum values with the Gd content of 1.0 wt.%. It has been reported that the larger R_f value corresponds to the denser oxide film which can effectively prevent the alloy from being eroded by corrosive medium [22], and the alloy with larger R_L value is not prone to pitting corrosion [34]. The results reveal that the addition of trace Gd can promote the formation of dense oxide film on the alloy surface and reduce the tendency of pitting corrosion. As-homogenized LAZ832−1.0Gd−0.2Zr alloy has the largest R_f and R_L values, indicating that this alloy shows the densest oxide film and is not prone to pitting corrosion.

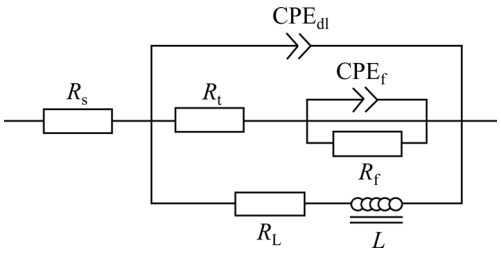

Fig. 9 Equivalent circuit used for fitting EIS of as-homogenized LAZ832−xGd−0.2Zr alloys

Figure 10 shows the hydrogen evolution of as-homogenized LAZ832−xGd−0.2Zr alloys immersed in 3.5 wt.% NaCl solution for 15 d. Clearly, the amount of hydrogen evolution increases with the increase of immersion time, and decreases first and then increases with the increase of Gd content. After immersing for 15 d, the hydrogen evolution volume of as-homogenized LAZ832−1.0Gd−0.2Zr alloy is the least of 5.0 mL/cm^2, while that of as-homogenized LAZ832−2.5Gd−0.2Zr

Table 5 EIS fitting results of as-homogenized LAZ832−xGd−0.2Zr alloys

Gd content/ wt.%	R_s/ (Ω·cm^2)	R_t/ (Ω·cm^2)	Y_{dl}/ (Ω^{-1}·cm^{-2}·s^n)	n_{dl}	R_f/ (Ω·cm^2)	Y_f/ (Ω^{-1}·cm^{-2}·s^n)	n_f	R_L/ (Ω·cm^2)	L/ (Ω·cm^2·s)
0	11.55	842.4	2.03×10^{-5}	0.86	410.8	2.44×10^{-3}	0.83	1153.0	4.41×10^{5}
0.5	7.08	936.9	1.71×10^{-5}	0.87	462.1	1.68×10^{-3}	0.75	1759.2	5.41×10^{5}
1.0	17.72	994.6	1.86×10^{-5}	0.83	480.5	1.61×10^{-3}	0.83	1993.6	6.23×10^{5}
1.5	5.61	880.1	2.05×10^{-5}	0.85	424.0	1.68×10^{-3}	0.90	1658.2	3.56×10^{5}
2.0	4.24	818.5	1.90×10^{-5}	0.86	376.7	2.16×10^{-3}	0.83	1097.9	4.67×10^{5}
2.5	5.58	766.0	1.73×10^{-5}	0.87	342.2	1.95×10^{-3}	0.76	945.4	5.12×10^{5}

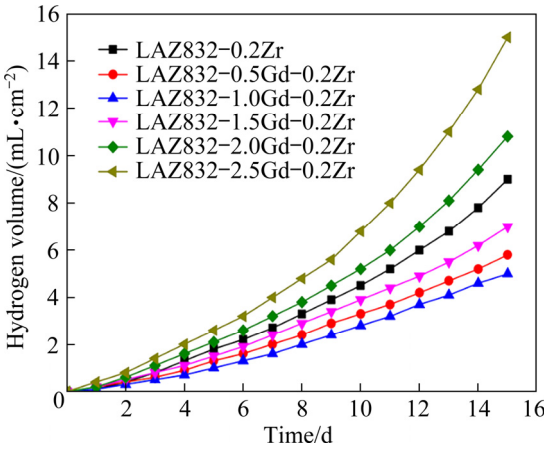

Fig. 10 Hydrogen evolution of as-homogenized LAZ832−*x*Gd−0.2Zr alloys immersed in 3.5 wt.% NaCl solution for 15 d

alloy is the largest of 15.0 mL/cm^2. Hydrogen evolution can be used to evaluate the dissolution rate of Mg alloy, because the collected hydrogen gas comes from cathodic hydrogen evolution reaction and the dissolution of 1 mol Mg generates 1 mol hydrogen gas [35]. Thus, the dissolution rates of as-homogenized LAZ832−*x*Gd−0.2Zr alloys are in ascending order of LAZ832−1.0Gd−0.2Zr < LAZ832−0.5Gd−0.2Zr < LAZ832−1.5Gd−0.2Zr < LAZ832−0.2Zr < LAZ832−2.0Gd−0.2Zr < LAZ832−2.5Gd−0.2Zr. As-homogenized LAZ832−1.0Gd−0.2Zr alloy has the lowest anodic dissolution rate and the best corrosion resistance, and this result is consistent with that obtained by electrochemical tests.

Polarization curves, impedance spectroscopy, and hydrogen evolution can well reflect the corrosion resistance of alloy. For comparison, the experimental parameters obtained from different methods are converted to corrosion rate by the following equations [36,37]:

$$P_J=22.85J_{corr} \quad (1)$$

$$P_{EIS}=22.85\frac{\beta_c\beta_a}{2.3R_P(\beta_c-\beta_a)} \quad (2)$$

$$P_H=3.96\frac{V_H}{\rho} \quad (3)$$

where P_J, P_{EIS}, and P_H are the corrosion rates determined using the corrosion current density (J_{corr}) from polarization curve, the polarization resistance (R_P) from impedance spectroscopy, and the hydrogen evolution rate (V_H) from hydrogen evolution, respectively. β_a and β_c are the anodic and cathodic Tafel slopes, respectively. ρ is the density of alloy. According to the equivalent circuit in Fig. 9, the R_P values of the alloys can be estimated by $1/R_P=1/(R_t+R_f)+1/R_L$, and calculated results are consistent with those obtained by the extrapolation of EIS data [38]. Table 6 presents the corrosion rates evaluated from polarization curves, EIS, and hydrogen evolution. Obviously, the corrosion rates evaluated by different methods reflect the same corrosion resistance results, that is, as-homogenized LAZ832−1.0Gd−0.2Zr alloy has the lowest corrosion rate and exhibits the best corrosion resistance. P_J and P_{EIS} are instantaneous corrosion rates without immersion test, while P_H is the average corrosion rate for 15-day immersion test. The P_H values of the alloys are higher than P_J and P_{EIS} values, but the difference is not significant. This suggests that the corrosion rates of as-homogenized LAZ832−*x*Gd−0.2Zr alloy do not increase significantly after long-term immersion.

Figure 11 shows the corrosion morphologies without corrosion products of as-homogenized LAZ832−*x*Gd−0.2Zr alloys immersed in 3.5 wt.% NaCl solution for 1 h. It can be seen that the *β*-Li phase of all alloys is preferentially corroded and

Table 6 Corrosion rates evaluated from polarization curves, EIS, and hydrogen evolution

Gd content/ wt.%	J_{corr}/ (μA·cm^{-2})	P_J/(mm·a^{-1})	R_p/(Ω·cm^2)	P_{EIS}/ (mm·a^{-1})	V_H (15 d)/ (mL·cm^{-2}·d^{-1})	P_H (15 d)/ (mm·a^{-1})
0	51.20	1.17	600.51	0.65	0.60	1.56
0.5	17.08	0.39	779.28	0.27	0.39	1.01
1.0	16.28	0.37	847.80	0.22	0.33	0.86
1.5	38.04	0.87	729.99	0.37	0.47	1.20
2.0	53.47	1.22	572.24	0.99	0.72	1.85
2.5	88.64	1.55	510.17	1.05	1.00	2.55

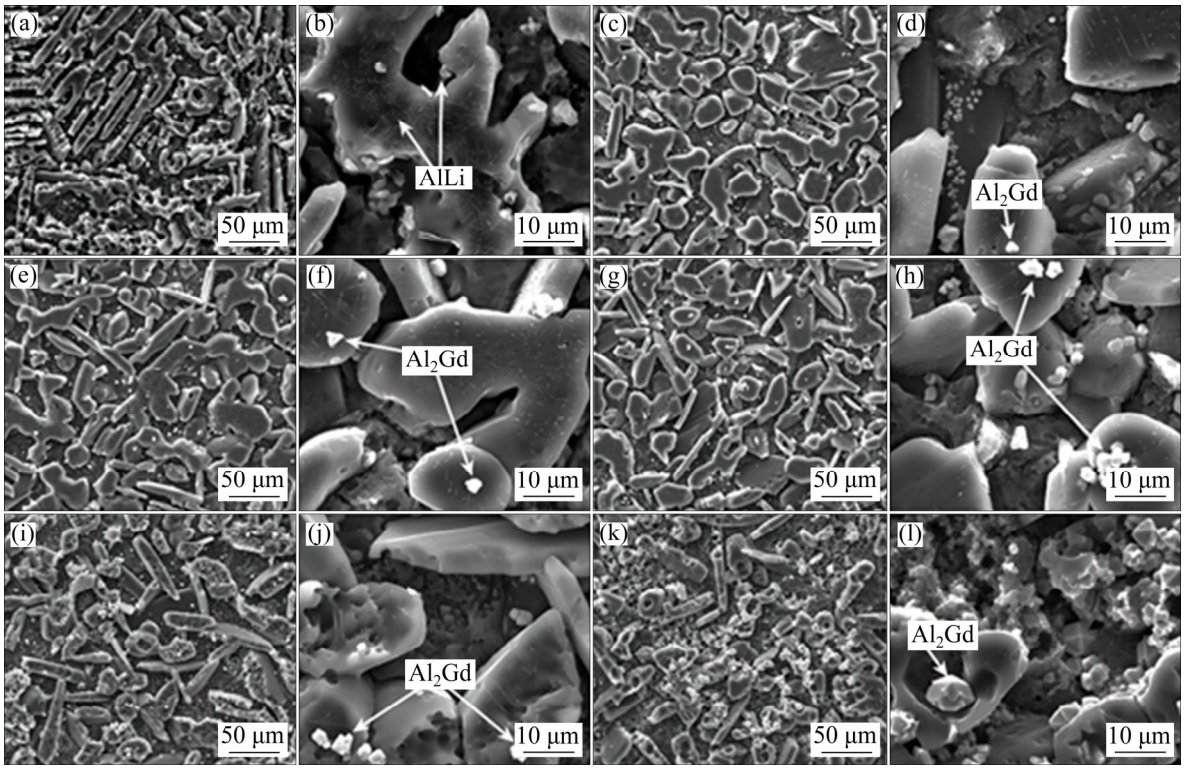

Fig. 11 Corrosion morphologies without corrosion products of as-homogenized LAZ832−*x*Gd−0.2Zr alloys immersed in 3.5 wt.% NaCl solution for 1 h: (a, b) *x*=0; (c, d) *x*=0.5; (e, f) *x*=1.0; (g, h) *x*=1.5; (i, j) *x*=2.0; (k, l) *x*=2.5

deep grove is left in its original position, while the *α*-Mg phase is protected to a certain extent, showing typical galvanic corrosion characteristics. In as-homogenized LAZ832−0.2Zr alloy, there are some corrosion pits on the surface of *α*-Mg matrix, and residual filamentous AlLi phase can be observed in corrosion pits. Compared with as-homogenized LAZ832−0.2Zr alloy, the surfaces of *α*-Mg matrix in as-homogenized LAZ832−0.5Gd−0.2Zr, LAZ832−1.0Gd−0.2Zr, and LAZ832−1.5Gd−0.2Zr alloys are smoother without obvious corrosion pits, and complete filamentous AlLi phase and polygonal Al_2Gd phase can be observed on the surface. Among them, the *α*-Mg matrix around segregated Al_2Gd phase is slightly corroded in as-homogenized LAZ832−1.5Gd−0.2Zr alloy. When the Gd element increases to 2.0 and 2.5 wt.%, the *α*-Mg matrix around segregated Al_2Gd phase is seriously corroded, and obvious corrosion pits appear on the surface of *α*-Mg matrix. Therefore, the addition of trace Gd element can effectively protect *α*-Mg matrix from corrosion and thereby improve the corrosion resistance of LAZ832−0.2Zr alloy. When the Gd content is 1.0 wt.%, the improvement effect is the most obvious.

Figure 12 shows the corrosion morphologies with corrosion products of as-homogenized LAZ832−*x*Gd−0.2Zr alloys immersed in 3.5 wt.% NaCl solution for 24 h. In as-homogenized LAZ832−0.2Zr alloy, there are white and loose oxidation products on the local surface of *β*-Li matrix, and a large number of microcracks almost cover the surface of *β*-Li matrix. In as-homogenized LAZ832−0.5Gd−0.2Zr alloy, no obvious white oxidation products are observed, but many microcracks still distribute on the surface of *β*-Li matrix. Compared with as-homogenized LAZ832−0.2Zr alloy, the number and size of microcracks on the *β*-Li matrix in as-homogenized LAZ832−0.5Gd−0.2Zr alloy are reduced, the *α*-Mg matrix is smoother without microcracks, and the filamentous AlLi phase and polygonal Al_2Gd phase are clearly visible. When the Gd content is 1.0 wt.%, the number and size of microcracks on *β*-Li matrix are further reduced, and the whole matrix surface presents a smooth and dense oxide film. Compared with as-homogenized LAZ832−1.0Gd−0.2Zr alloy, the number and size of microcracks on *β*-Li matrix in as-homogenized LAZ832−1.5Gd−0.2Zr alloy are increased, but the *α*-Mg matrix is still smooth

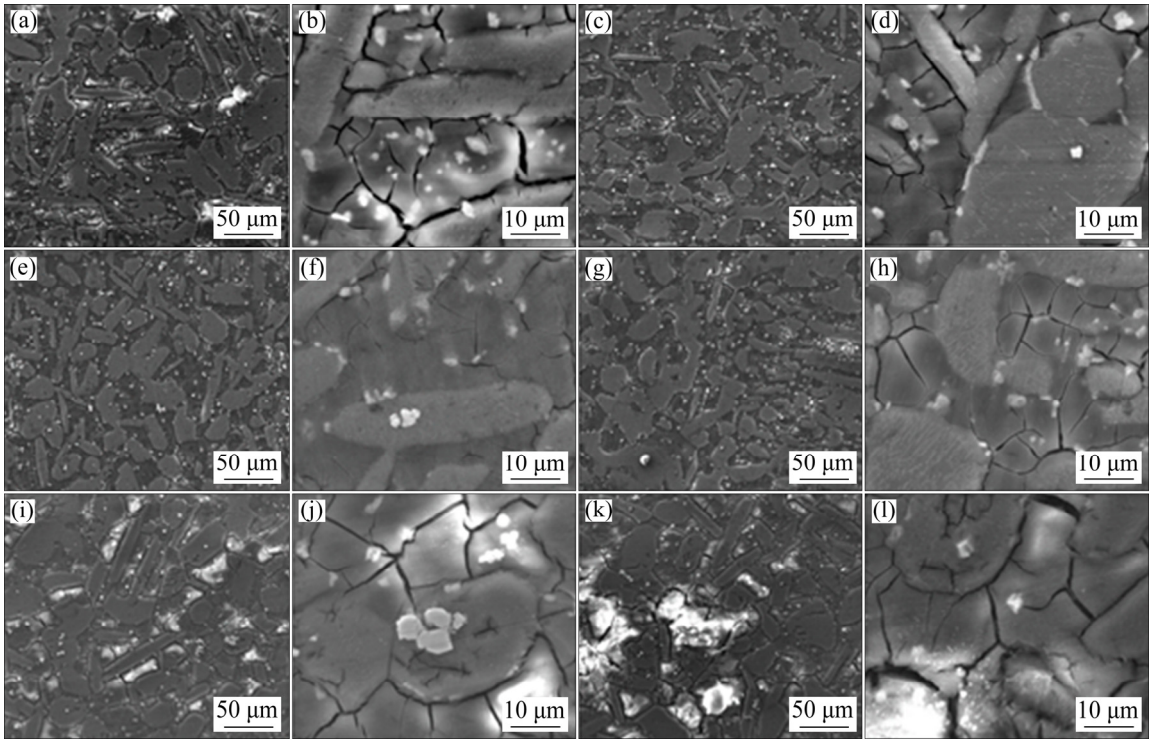

Fig. 12 Corrosion morphologies with corrosion products of as-homogenized LAZ832−*x*Gd−0.2Zr alloys immersed in 3.5 wt.% NaCl solution for 24 h: (a, b) *x*=0; (c, d) *x*=0.5; (e, f) *x*=1.0; (g, h) *x*=1.5; (i, j) *x*=2.0; (k, l) *x*=2.5

without microcracks. When the Gd content further increases to 2.0 and 2.5 wt.%, more and more white oxidation products appear on the alloy surface, the number and size of microcracks on β-Li matrix increase, and many microcracks gradually appear on the surface of α-Mg matrix. The results show that the addition of trace Gd element is beneficial to the formation of dense oxide film on alloy surface, while the addition of excessive Gd element promotes more serious corrosion. This is consistent with the result that the R_f value increases first and then decreases with the increase of Gd content and reaches the maximum value when the Gd content is 1.0 wt.%, and it has been reported that the addition of RE elements can promote the formation of dense oxide film on the surfaces of Mg−Li alloys [21,22].

Figure 13 presents the XPS spectra of surface oxide films on as-homogenized LAZ832−0.2Zr alloy and LAZ832−1.0Gd−0.2Zr alloy immersed in 3.5 wt.% NaCl solution for 24 h. The XPS spectra are analyzed by Avantage software combined with NIST XPS database [39]. The Mg 2p peaks of the two alloys are divided into four peaks of Mg, $Mg(OH)_2$, MgO, and MgO/Mg, while the Li 1s peaks are undetected in both two alloys. It should be noted that LiOH is not easily detected on the oxide film due to its high solubility in water, so the corrosion products may contain LiOH. The Al 2s peak of LAZ832 alloy without Zr contains two peaks of Al and Al_2O_3, while that of LAZ832−1.0Gd−0.2Zr alloy only contains Al_2O_3 peak. The Zn 2p peaks are detected in the two alloys, and can be described with ZnO and $ZnAl_2O_4$. The Gd 3d peak is undetected in LAZ832−0.2Zr alloy, but it is visible in LAZ832−1.0Gd−0.2Zr alloy and only contains Gd_2O_3 peak. Therefore, the oxide films of the two alloys contain MgO, $Mg(OH)_2$, Al_2O_3, ZnO and $ZnAl_2O_4$. Besides, the oxide film of LAZ832−1.0Gd−0.2Zr alloy also contains a small amount of Gd_2O_3. This indicates that the addition of Gd results in the formation of oxide film containing Gd_2O_3, which is in agreement with the study of ATHUL et al [31].

In conclusion, the addition of trace Gd can effectively improve the corrosion resistance of as-homogenized LAZ832−0.2Zr alloy, and the best corrosion resistance is obtained when the Gd content is 1.0 wt.%. This can be explained by phase composition, microstructure, and oxide film. First, Gd as a rare earth element can remove impurities and purify the melt in as-homogenized LAZ832−0.2Zr alloy, and thereby reduce the galvanic

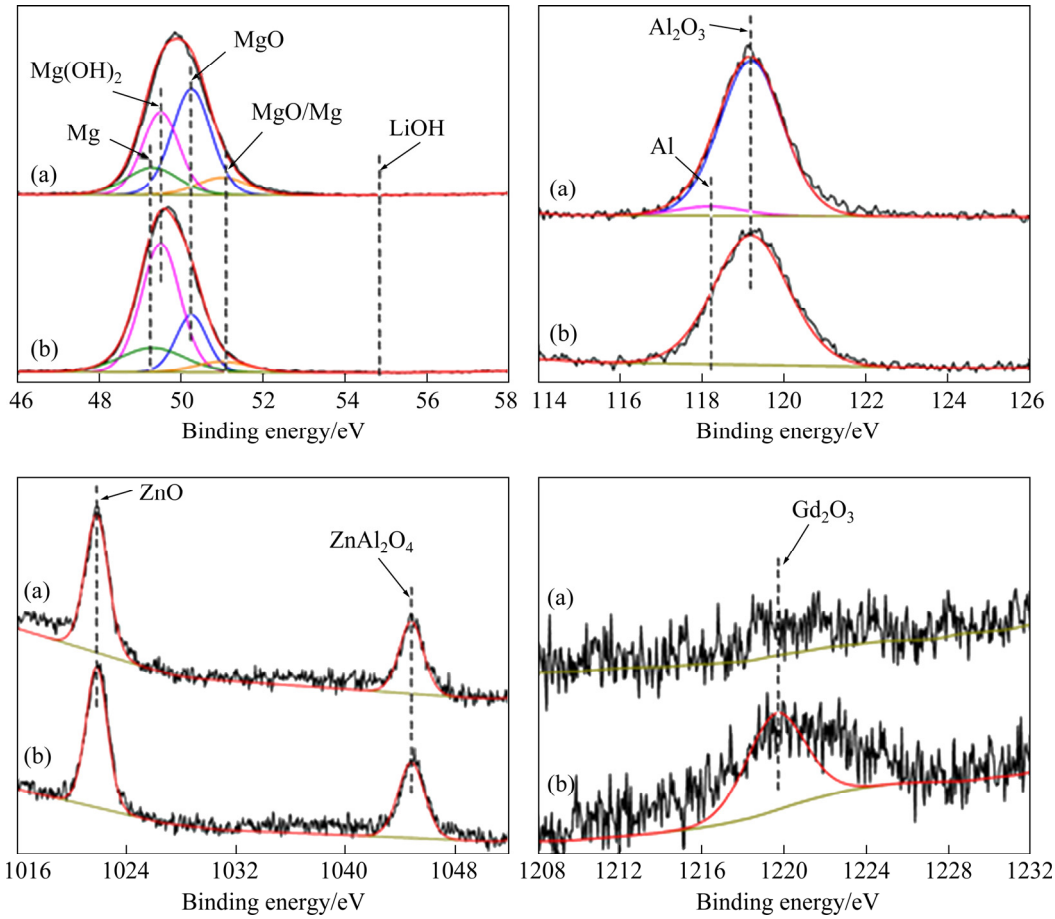

Fig. 13 XPS spectra of surface oxide films on as-homogenized LAZ832−0.2Zr (a) and LAZ832−1.0Gd−0.2Zr (b) alloys immersed in 3.5 wt.% NaCl solution for 24 h

corrosion between alloy matrix and impurities, which is conducive to improving the corrosion resistance of the alloy. Second, the second phase has a significant effect on the corrosion resistance of Mg alloys, and most of elements play an important role after the formation of second phase. AlLi phase has a more negative electrode potential than α-Mg and β-Li matrix phases, which leads to microgalvanic corrosion between AlLi phase and matrix phases, and AlLi phase as anode is corroded preferentially. The addition of trace Gd results in the formation of Al_2Gd phase and the decrease of AlLi content, accordingly weakening the microgalvanic corrosion between AlLi phase and matrix phases. In addition, Al_2Gd phase mainly distributes in α-Mg matrix and at the α-Mg/β-Li phase interface, and it has been reported that Al_2Gd phase has more positive electrode potential than α-Mg phase [40]. The potential difference between β-Li matrix and Al_2Gd phase is larger than that between α-Mg matrix and Al_2Gd phase, so that the Al_2Gd phase distributing at α-Mg/β-Li phase interface has the priority to establish microgalvanic couples with β-Li matrix, which can effectively inhibit the galvanic corrosion between α-Mg phase and β-Li phase and protect the original morphology of α-Mg matrix from erosion (Fig. 11(f)). Therefore, the formation of Al_2Gd phase and decrease of AlLi content are beneficial to the corrosion resistance of alloy, and this is also the main reason why the addition of trace Gd can reduce the corrosion current density and increase the charge transfer resistance of alloy. Previous studies have shown that other rare earth elements (such as Ce, Y, and Nd) have similar effects on Mg−Li−Al base alloys [21−23]. The Al_2Gd phases distributing in α-Mg matrix establish microgalvanic couples with α-Mg matrix, and corrosion occurs preferentially in the α-Mg matrix around Al_2Gd phase. The segregation of Al_2Gd phase caused by the addition of excessive Gd element leads to serious corrosion of surrounding α-Mg matrix (Figs. 11(h, j, l)), which is the main reason for the deterioration of corrosion resistance after adding excessive Gd.

Finally, oxide film also has a significant effect on the corrosion resistance of alloy, and its stability depends on the Pilling−Bedworth ratio (PBR) and standard enthalpy of corresponding compounds, as listed in Table 7. The oxide films of both as-homogenized LAZ832−0.2Zr and LAZ832−1.0Gd−0.2Zr alloys contain MgO, $Mg(OH)_2$, Al_2O_3, ZnO, $ZnAl_2O_4$, and perhaps LiOH. Besides, Gd_2O_3 is detected in the oxide film of LAZ832−1.0Gd−0.2Zr alloy. Among these compounds, MgO, $Mg(OH)_2$, LiOH, and ZnO have higher standard enthalpy and show poor chemical stability, which cannot provide effective protection for alloy matrix. For $ZnAl_2O_4$, although the PBR and standard enthalpy are not available, it has been reported that the oxide film containing $ZnAl_2O_4$ can effectively improve the corrosion resistance of alloy [41]. This is because $ZnAl_2O_4$ has excellent corrosion resistance and can be filled into the pores of oxide film, so as to reduce the porosity of oxide film and improve the density of oxide film. Both Al_2O_3 and Gd_2O_3 have moderate PBR (between 1 and 2) and lower standard enthalpy, exhibiting a good protective effect on alloy. Therefore, the formation of Gd_2O_3 is the main reason for the densest oxide film on as-homogenized LAZ832−1.0Gd−0.2Zr alloy.

Table 7 PBR and standard enthalpy of related compounds

Compound	PBR	Enthalpy/(kJ·mol^{-1})
MgO	0.8	−601.7
$Mg(OH)_2$	1.8	−924.66
LiOH	1.26	−484.93
Al_2O_3	1.28	−1669.8
ZnO	1.62	−350.5
Gd_2O_3	1.23	−1819.6

4 Conclusions

(1) As-homogenized LAZ832−0.2Zr contains α-Mg, β-Li, AlLi, and $MgLi_2Al$ phases. The addition of Gd results in the formation of Al_2Gd and the decrease of AlLi content. The addition of trace Gd can effectively refine the microstructure of alloy and make the long-strip α-Mg phase change to round-like shape, while the addition of excessive Gd leads to coarsening of α-Mg phase and segregation of Al_2Gd phase.

(2) With the increase of Gd content, both the tensile strength and elongation LAZ832−xGd−0.2Zr alloys increase first and then decrease. As-homogenized LAZ832−1.0Gd−0.2Zr alloy has the best mechanical properties (UTS=189.8 MPa and δ=42.3%), which is mainly attributed to the refinement of microstructure, the decrease of AlLi content, and the formation of Al_2Gd phase.

(3) The addition of trace Gd improves the corrosion resistance of alloy, and as-homogenized LAZ832−1.0Gd−0.2Zr alloy exhibits the best corrosion resistance. The reason is that the decrease of AlLi content weakens the microgalvanic corrosion between AlLi phase and matrix phases, the formation of Al_2Gd phase effectively inhibits the galvanic corrosion between α-Mg phase and β-Li phase, and the addition of trace Gd makes the compact oxide film containing Gd_2O_3 on the alloy surface.

Acknowledgments

The authors are grateful for the financial supports from the Anhui Provincial Natural Science Foundation, China (No. 2208085QE124), the Natural Science Foundation of the Education Department of Anhui Province, China (No. KJ2021A0394), and the Open Project of Key Laboratory of Green Fabrication and Surface Technology of Advanced Metal Materials, China (No. GFST2021KF04).

References

[1] XU W, BIRBILIS N, SHA G, WANG Y, DANIELS J E, XIAO Y, FERRY M. A high-specific-strength and corrosion-resistant magnesium alloy [J]. Nature Materials, 2015, 14(12): 1229−1235.

[2] FU Hui, GE Bin-cheng, XIN Yun-chang, WU Rui-zhi, FERNANDEZ C, HUANG Jian-yu, PENG Qiu-ming. Achieving high strength and ductility in magnesium alloys via densely hierarchical double contraction nanotwins [J]. Nano Letters, 2017, 17: 6117−6124.

[3] SUN Yue-hua, WANG Ri-chu, PENG Chao-qun, FENG Yan, YANG Ming. Corrosion behavior and surface treatment of superlight Mg−Li alloys [J]. Transactions of Nonferrous Metals Society of China, 2017, 27(7): 1455−1475.

[4] DING Hong-bo, LIU Qiang, ZHOU Hai-tao, ZHOU Xiao, ATRENS A. Effect of thermal-mechanical processing on microstructure and mechanical properties of duplex-phase Mg−8Li−3Al−0.4Y alloy [J]. Transactions of Nonferrous Metals Society of China, 2017, 27(12): 2587−2597.

[5] WU R, YAN Y, WANG G, MURR L E, HAN W, ZHANG Z, ZHANG M. Recent progress in magnesium−lithium

alloys [J]. International Materials Reviews, 2015, 60(2): 65−100.

[6] ZHANG Cheng, WU Liang, ZHAO Zi-long, XIE Zhi-hui, HUANG Guang-sheng, LIU Lei, JIANG Bin, ATRENS A, PAN Fu-sheng. Effect of Li content on microstructure and mechanical property of Mg−*x*Li−3(Al−Si) alloys [J]. Transactions of Nonferrous Metals Society of China, 2019, 29(12): 2506−2513.

[7] ZHU Tian-long, CUI Chong-liang, ZHANG Tian-long, WU Rui-zhi, BETSOFEN S, LENG Zhe, ZHANG Jing-huai, ZHANG Mi-lin. Influence of the combined addition of Y and Nd on the microstructure and mechanical properties of Mg−Li alloy [J]. Materials & Design, 2014, 57: 245−249.

[8] ZHAO Zi-long, CHEN Jun-xian, WU Xin, LIU Fa-qian. Design of a Mg−7Li−2.6Al−0.4Si alloy with simultaneous improved strength and ductility [J]. Materials Today Communication, 2021, 27: 102244.

[9] PUGAZHENDHI B S, KAR A, SINNAERUVADI K, SUWAS S. Effect of aluminium on microstructure, mechanical properties and texture evolution of dual phase Mg−8Li alloy in different processing conditions [J]. Archives of Civil and Mechanical Engineering, 2018, 18(4): 1332−1344.

[10] ZHAO Zi-long, DUAN Bao-yu, YING Jie, LI Liang. Effect of Al addition on microstructure and tensile properties of Mg−8Li−3Al alloy [J]. JOM, 2021, 73(8): 1−7.

[11] ZHAO Zi-long, SUN Zi-wei, LIANG Wei, WANG Yi-de, BIAN Li-ping. Influence of Al and Si additions on the microstructure and mechanical properties of Mg−4Li alloys [J]. Materials Science and Engineering A, 2017, 702: 206−217.

[12] GUSIEVA K, DAVIES C H J, SCULLY J R, BIRBILIS N. Corrosion of magnesium alloys: The role of alloying [J]. International Materials Reviews, 2015, 60(3): 169−194.

[13] CAO Dian-xue, WU Lin, SUN Yong, WANG Gui-ling, LV Yan-zhuo. Electrochemical behavior of Mg−Li, Mg−Li−Al and Mg−Li−Al−Ce in sodium chloride solution [J]. Journal of Power Source, 2008, 177(2): 624−630.

[14] WU Rui-zhi, QU Zhi-kun, ZHANG Mi-lin. Reviews on the influences of alloying elements on the microstructure and mechanical properties of Mg−Li base alloys [J]. Reviews on Advanced Materials Science, 2010, 24(1): 35−43.

[15] TANG Yan, JIA Wei-tao, LIU Xuan, LE Qi-chi, ZHANG Yu-lei. Fabrication of high strength α, $\alpha+\beta$, β phase containing Mg−Li alloys with 0.2% by extruding and annealing process [J]. Materials Science and Engineering A, 2016, 675: 55−64.

[16] SUN Yue-hua, WANG Ri-chu, REN Jian, PENG Chao-qun, CAI Zhi-yong. Microstructure, texture, and mechanical properties of as-extruded Mg−*x*Li−3Al−2Zn−0.2Zr alloys (*x*= 5, 7, 8, 9, 11 wt.%) [J]. Materials Science and Engineering A, 2019, 755: 201−210.

[17] SUN Yue-hua, WANG Ri-chu, PENG Chao-qun, WANG Xiao-feng. Microstructure and corrosion behavior of as-homogenized Mg−*x*Li−3Al−2Zn−0.2Zr alloys (*x*=5, 8, 11 wt.%) [J]. Materials Characterization, 2020, 159: 110031.

[18] SUN Yue-hua, WANG Ri-chu, PENG Chao-qun, CAI Zhi-yong. Microstructure and corrosion behavior of as-extruded Mg−*x*Li−3Al−2Zn−0.2Zr alloys (*x*=5, 8, 11 wt.%) [J]. Corrosion Science, 2020, 167: 108487.

[19] ZHAO Jiong, ZHANG Jie, LIU Wen-cai, WU Guo-hua, ZHANG Liang. Effect of Y content on microstructure and mechanical properties of as-cast Mg−8Li−3Al−2Zn alloy with duplex structure [J]. Materials Science and Engineering A, 2016, 650: 240−247.

[20] ZHANG Jie, ZHANG Yang, WU Guo-hua, LIU Wen-cai, ZHANG Liang, DING Wen-jiang. Microstructure and mechanical properties of as-cast and extruded Mg−8Li−3Al−2Zn−0.5Nd alloy [J]. Materials Science and Engineering A, 2015, 621: 198−203.

[21] GU M, WEI G L, ZHAO J J, LIU W, WU G H. Influence of yttrium addition on the corrosion behaviour of as-cast Mg−8Li−3Al−2Zn alloy [J]. Materials Science and Technology, 2016: 1−6.

[22] GU M Y, WEI G L, LIU W C, WU G H. Influence of neodymium on microstructure and corrosion behavior of Mg−8Li−3Al−2Zn alloy [J]. Materials and Corrosion, 2017, 68(4): 436−443.

[23] MANIVANNAN S, DINESH P, MAHEMAA R, MARIYAPILLAI N, BABU S P K, SUNDARRAJAN S. Corrosion behavior of as-cast Mg−8Li−3Al+*x*Ce alloy in 3.5wt.% NaCl solution [J]. International Journal of Minerals, Metallurgy and Materials, 2016, 23(10): 1196−1203.

[24] MASSALSKI T B, OKAMOTO H, SUBRAMANIAN P R, KACPRZAK L. Binary alloy phase diagrams [M]. Ohio: ASM International, 1990.

[25] WU Rui-zhi, QU Zhi-kun, ZHANG Mi-lin. Effects of the addition of Y in Mg−8Li−(1,3)Al alloy [J]. Materials Science and Engineering A, 2009, 516: 96−99.

[26] SINGH L K, BHADAURIA A, SRINIVASAN A, PILLAI U T S, PAI B C. Effects of gadolinium addition on the microstructure and mechanical properties of Mg−9Al alloy [J]. International Journal of Minerals, Metallurgy and Materials, 2017, 24(8): 901−908.

[27] FEI Peng-fei, QU Zhi-kun, WU Rui-zhi. Microstructure and hardness of Mg−9Li−6Al−*x*La (*x*=0, 2, 5) alloys during solid solution treatment [J]. Materials Science and Engineering A, 2015, 625: 169−176.

[28] QU Zhi-kun, WU Rui-zhi, ZHAN Hai-bo, ZHANG Mi-lin. The solution and room temperature aging behavior of Mg−9Li−*x*Al (*x*=3, 6) alloys [J]. Journal of Alloys and Compounds, 2012, 536: 145−149.

[29] WU Rui-zhi, ZHANG Mi-lin. Microstructure, mechanical properties and aging behavior of Mg−5Li−3Al−2Zn−*x*Ag [J]. Materials Science and Engineering A, 2009, 520: 36−39.

[30] ZHAO Jiong, LI Zhong-quan, LIU Wen-cai, ZHANG Jie, ZHANG Liang, TIAN Ying, WU Guo-hua. Influence of heat treatment on microstructure and mechanical properties of as-cast Mg−8Li−3Al−2Zn−*x*Y alloy with duplex structure [J]. Materials Science and Engineering A, 2016, 669: 87−94.

[31] ATHUL K P, SRINIVASAN A, PILLAI U T S. Investigations on the microstructure, mechanical, corrosion and wear properties of Mg−9Al−*x*Gd (0, 0.5, 1, and 2 wt.%) alloys [J]. Journal of Materials Research, 2017, 32: 3732−3743.

[32] ZHANG Tao, SHAO Ya-wei, MENG Guo-zhe, CUI Zhong-yu, WANG Fu-hui. Corrosion of hot extrusion AZ91 magnesium alloy: I-relation between the microstructure and

corrosion behavior [J]. Corrosion Science, 2011, 53(5): 1960−1968.
[33] LIU Xuan, XUE Ji-lai, LIU Shi-zhe. Discharge and corrosion behaviors of the α-Mg and β-Li based Mg alloys for Mg-air batteries at different current densities [J]. Materials & Design, 2018, 160: 138−146.
[34] NAKATSUGAWA I, MARTIN R, KNYSTAUTAS E J. Improving corrosion resistance of AZ91D magnesium alloy by nitrogen ion implantation [J]. Corrosion Science, 1996, 52(12): 921−926.
[35] LI C Q, XU D K, CHEN X B, WANG B J, WU R Z, HAN E H, BIRBILIS N. Composition and microstructure dependent corrosion behaviour of Mg−Li alloys [J]. Electrochimica Acta, 2018, 260: 55−64.
[36] SHI Z, LIU M, ATRENS A. Measurement of the corrosion rate of magnesium alloys using Tafel extrapolation [J]. Corrosion Science, 2010, 52(2): 579−588.
[37] KING A D, BIRBILIS N, SCULLY J R. Accurate electrochemical measurement of magnesium corrosion rates; a combined impedance, mass-loss and hydrogen collection study [J]. Electrochimica Acta, 2014, 121: 394−406.
[38] ATRENS A, SONG G L, LIU M, SHI Z, CAO F, DARGUSH M S. Review of recent developments in the field of magnesium corrosion [J]. Advanced Engineering Materials, 2015, 17(4): 400−453.
[39] NAUMKIN A V, KRAUT-VASS A, GAARENSTROOM S W, POWELL C J. NIST X-ray photoelectron spectroscopy database 20 [EB/OL]. Version 4.1, 2012. http://dx.doi.org/10.18434/T4T88K.
[40] LU Fu-min, MA Ai-bin, JIANG Jing-hua, GUO Yu, YANG Dong-hui, SONG Dan, CHEN Jian-qing. Significantly improved corrosion resistance of heat-treated Mg−Al−Gd alloy containing profuse needle-like precipitates within grains [J]. Corrosion Science, 2015, 94: 171−178.
[41] FAN Guo-li, LI Feng. In situ crystallization to zinc aluminate films with controlled surface microstructure and anticorrosion performance [J]. AlChE Journal, 2012, 58(9): 2639−2648.

稀土 Gd 对均匀化态 Mg−8Li−3Al−2Zn−0.2Zr 合金显微组织、力学性能和腐蚀行为的影响

孙月花[1]，王日初[2]，彭超群[2]，王小锋[2]

1. 安徽工业大学 材料科学与工程学院，马鞍山 243002；
2. 中南大学 材料科学与工程学院，长沙 410083

摘 要：通过显微组织观察、拉伸测试、电化学测试和腐蚀形貌表征等手段研究稀土 Gd 对均匀化态 Mg−8Li−3Al−2Zn−0.2Zr (LAZ832−0.2Zr)合金显微组织、力学性能和腐蚀行为的影响。结果表明：微量 Gd 的添加可细化显微组织、降低 AlLi 软化相的含量、生成 Al_2Gd 强化相，从而提高均匀化态 LAZ832−0.2Zr 合金的力学性能。同时，微量 Gd 的添加可弱化基体相与 AlLi 相之间的微电偶腐蚀、抑制 α-Mg 与 β-Li 基体相之间的电偶腐蚀、形成含 Gd_2O_3 的致密氧化膜，从而有效改善均匀化态 LAZ832−0.2Zr 合金的耐蚀性。当 Gd 含量为 1.0%(质量分数)时，合金表现出最佳的综合性能，其抗拉强度为 189.8 MPa，伸长率为 42.3%，腐蚀速率(由析氢实验获得)为 0.86 mm·a^{-1}。

关键词：Mg−Li 合金；稀土 Gd；显微组织；力学性能；腐蚀行为

(Edited by Bing YANG)